

Supplementary Information

Electrochemical Lithiation-induced Formation of Disordered Rocksalt

Matthew J A Leesmith¹, Nathan R Halcovitch¹, Xiao Hua^{1*}

¹ Department of Chemistry, Lancaster University, Lancaster LA1 4YB, UK

Corresponding author email address: x.hua1@lancaster.ac.uk

METHODS:

Materials:

The several metal oxides M_xO_y (β - MnO_2 , α - Mn_2O_3 , α - Fe_2O_3 , Cr_2O_3 and α - V_2O_5) were all purchased from Sigma-Aldrich. The synthesis of nanostructured β - MnO_2 followed a reported hydrothermal route¹. The electrodes were prepared in a form of self-standing films (of about 125 μm thickness) that contain 70 wt% active material, 10 wt% PTFE and 20 wt% Super P carbon (TIMCAL C65). The electrode pellets were punched out using a 3 mm (diameter) hole puncher with an average mass loading of about 2.0 mg. All films and electrode pellets were prepared in atmosphere. A Swagelok-type PFA *operando* cell was assembled in an Ar-filled glovebox (MBraun) using the as-prepared electrode pellets with a glass fibre (Whatman) as separator, a Li metal foil as counter electrode, and 1 M $LiPF_6$ in ethylene carbonate (EC) / dimethyl carbonate (DMC) solution (volume ratio 1:1) as electrolyte. The fully discharged and charged M_xO_y materials for *ex situ* X-ray total scattering measurement were cycled in coin cells. The coin cells were made in the same way as the *operando* cell. All cells were cycled at room temperature under a rate of C/20 unless specified. The Li content in the galvanostatic plots was derived based on the theoretical capacity of the full conversion reaction of the respective metal oxides. For the preparation of *ex situ* samples, all cells were stopped at selected voltages or states of (dis)charge, and were then transported and disassembled inside the Ar-filled glovebox. After disassembling, the pellets were rinsed with DMC twice before drying in the antechamber.

Characterisation:

The *operando* X-ray total scattering data of MnO_2 were collected at beamline I15-1 at the Diamond Light Source using an amorphous silicon area detector (Perkin Elmer, XRD4343CT) with an X-ray beam of energy 76.69 keV ($\lambda = 0.1617 \text{ \AA}$) and Q_{max} of 25 \AA^{-1} . Experiments were conducted in transmission geometry within the PFA Swagelok cell. An empty Swagelok cell was measured for the background. The *operando* electrochemistry was conducted using a rate of C/15. The *ex situ* X-ray total scattering data were collected in house using a single crystal diffractometer (Rigaku Oxford Diffraction SuperNova) equipped with a Mo source ($\lambda = 0.7107 \text{ \AA}$) and a CCD area detector (ATLAS-S2). A Q_{max} of $14\text{-}16 \text{ \AA}^{-1}$ was achieved. Experiments were conducted in transmission geometry with samples sealed in either Kapton tapes or capillaries. An additional empty tape and capillary were measured for background. Note that XRD data presented in this work have all been converted to Cu Ka wavelength for easy comparison with literature. Joint XRD and PDF refinements were performed using TOPAS software.

Metropolis non-negative matrix factorisation (MMF):

The MMF approach followed closely the same method reported earlier², which uses the Metropolis Monte Carlo algorithm to carry out non-negative matrix factorisation (NMF)³. The NMF analysis was

performed on renormalised PDFs to satisfy the non-negative criterion of NMF. The renormalised $g^{\text{exp}}(r)$ were derived from the experimental $G^{\text{exp}}(r)$ using equation $G(r) = 4\pi r \rho_0 (g(r) - 1)^4$, in which ρ_0 refers to the number density of the structure model. Three fundamental components $g_i^*(r)$ ($i = 3$) were employed in the analysis. The goal of the analysis was to identify these $g_i^*(r)$ and associated weights w_{ij} (j corresponds to the number of experimental $g_j^{\text{exp}}(r)$) to minimise $|g_j^{\text{calc}}(r) - g_j^{\text{exp}}(r)|^2$, where $g_j^{\text{calc}}(r) = \sum_{i=1}^3 w_{ij} g_i^*(r)$. Additional constraints were applied to ensure non-negative $g_i^*(r)$ for all i and r , and that $\sum_{i=1}^3 w_{ij} = 1$ for all j . The initial $g_1^*(r)$ representing the known component was fixed as the experimental function measured at the end of first discharge, whereas the two unknown components $g_2^*(r)$ and $g_3^*(r)$ and all w_{ij} were assigned randomly subject to the various constraints listed above. Each iteration involved random variation of these parameters, followed by the calculation of the change in $|g_j^{\text{calc}}(r) - g_j^{\text{exp}}(r)|^2$. The acceptance or rejection of the variation follows MMC algorithm. The variation was repeated under increasingly stringent acceptance criteria using simulated annealing until convergence was achieved.

FIGURES:

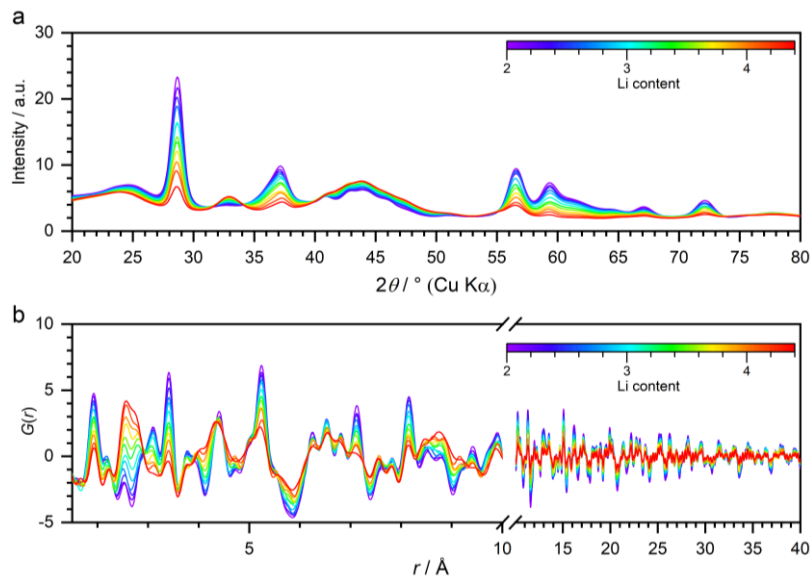


Figure S1 (a) XRD and **(b)** PDF data of the “conversion” regime ($\text{Li} \geq 2$) from the *operando* X-ray total scattering experiments.

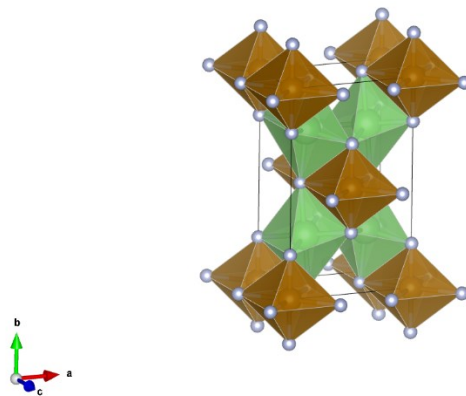


Figure S2 Crystal structure of $\text{Li}_{0.5}\text{MnO}_2$ ($Cmmm$) for the refinement. Oxygen anions are denoted by grey balls. Mn sites are denoted by brown octahedra. Green octahedra are shared by Li and Mn with a 1 : 1 ratio.

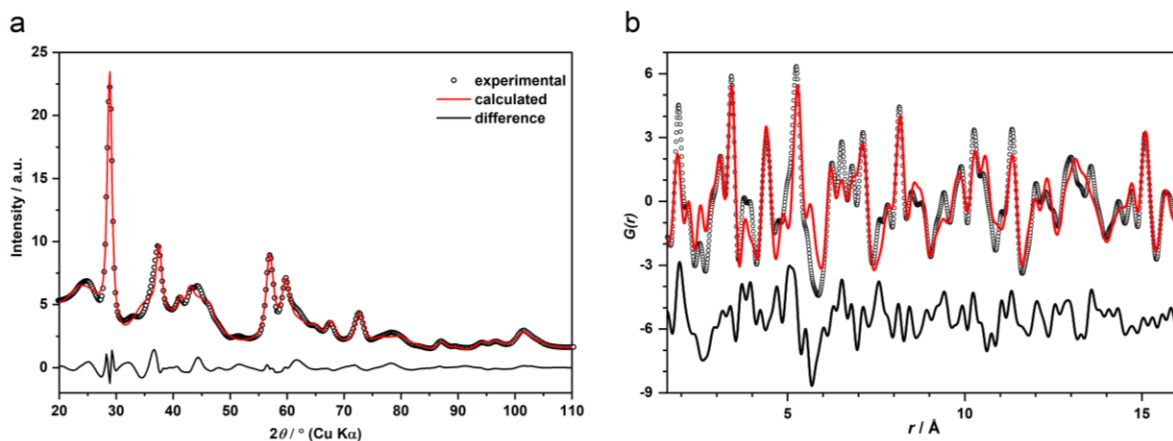


Figure S3 (a) XRD ($R_w = 5.7\%$) and **(b)** PDF ($R_w = 45\%$) joint refinement of *operando* Li 2.0 data using spinel phase (LiMn_2O_4 , $I4_1/amd$) for *gr3*.

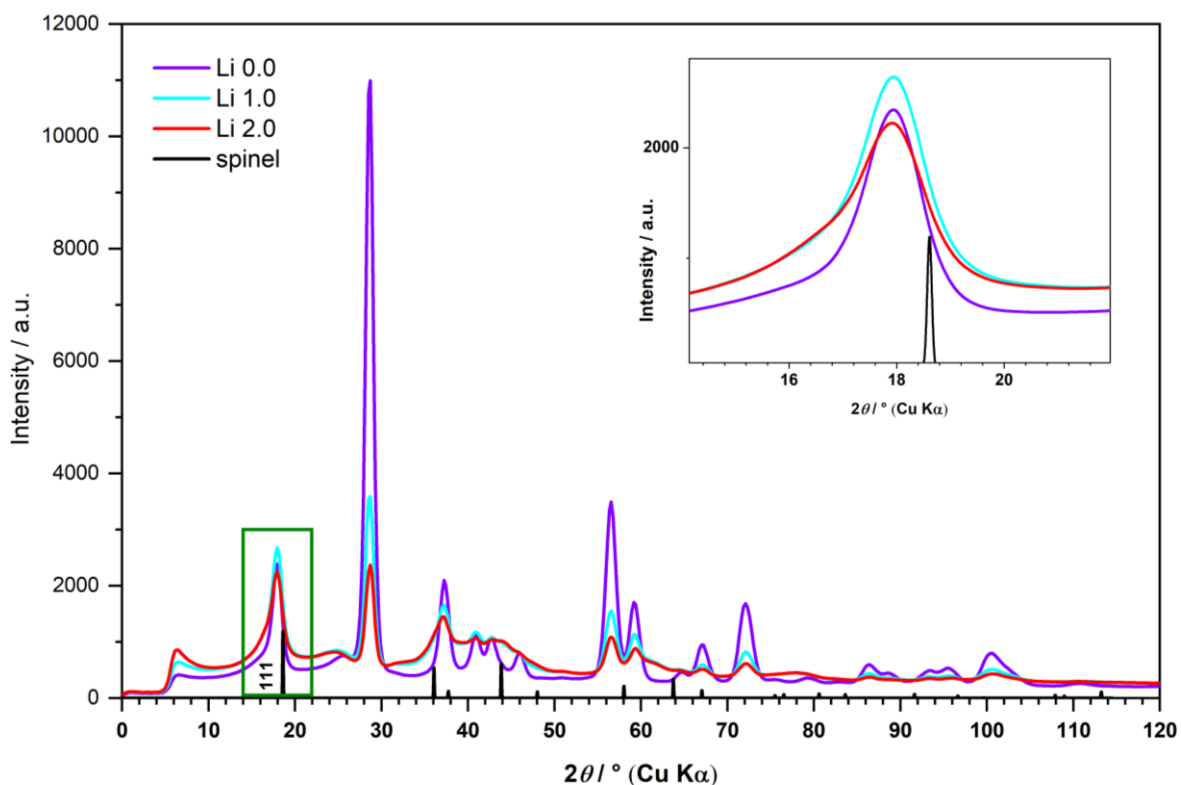


Figure S4 *Operando* X-ray total scattering data for Li 0 (purple), Li 1.0 (cyan) and Li 2.0 (red). Simulated XRD pattern of the spinel phase (LiMn_2O_4 , $I4_1/amd$) is shown for comparison. The inset highlights the main (111) reflection of spinel at low two-theta region for a clearer view. Whilst other reflections appear to have an overall good agreement between the simulation and experiment, the mismatch concerning this key peak is evident.

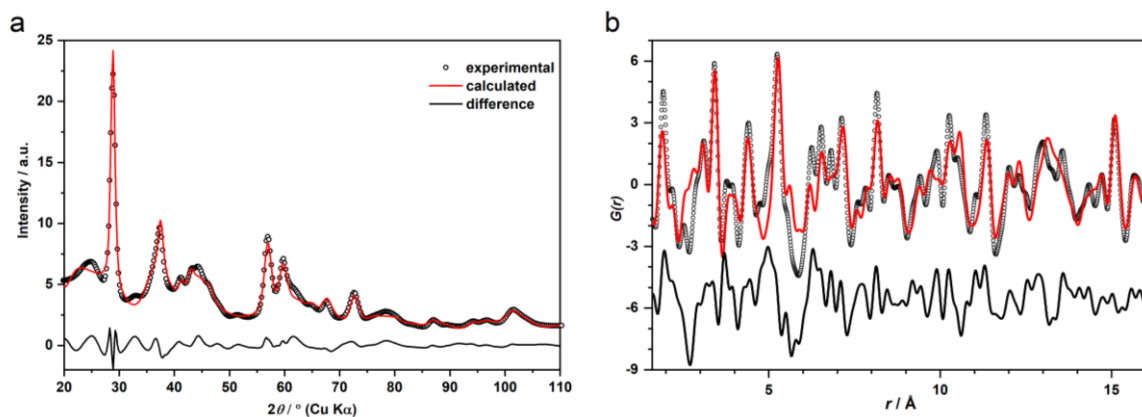


Figure S5 (a) XRD ($R_w = 6.6\%$) and (b) PDF ($R_w = 50\%$) joint refinement of *operando* Li 2.0 data excluding the interfacial $\text{Li}_{0.5}\text{MnO}_2$ ($Cmmm$) phase in the model. The refinement shows poor agreement with the experiment, in particularly for the PDF data, demonstrating that the two intermediates are structurally different and are both required to model the XRD and PDF data.

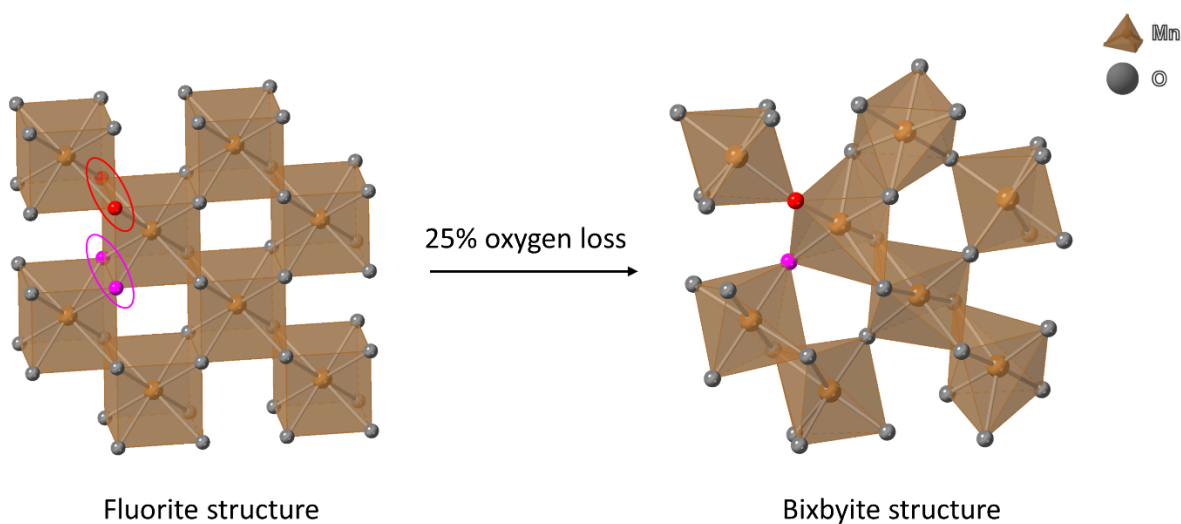


Figure S6 Relationship of the anion sublattice between fluorite (left) and bixbyite (right). The grey balls denote the anions (oxygen). Two sets of related O^{2-} in two structures are shown in the same colour.

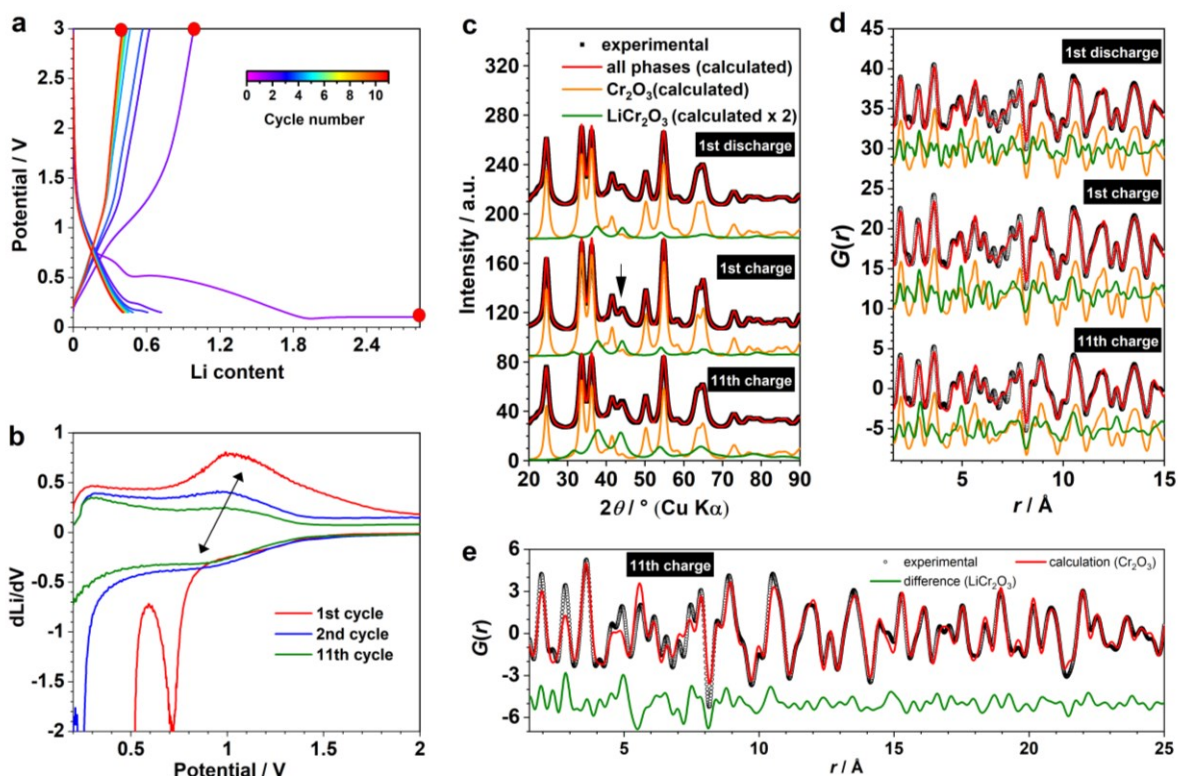


Figure S7 (a) The first 11 cycles of commercial Cr_2O_3 within voltage window of 0.15 – 3.0 V. Red balls denote the states of (dis)charge where samples were collected for *ex situ* XRD/PDF analysis. **(b)** Derivatives of the selected cycles from a. Black arrows mark the reversible processes associated with Cr redox during the (de)lithiation of DRX. Joint **(c)** XRD and **(d)** PDF refinement from the *ex situ* samples collected in a. Contributions from unreacted pristine (orange) and the DRX (green) phases in each sample is shown. Note that the intensity from the DRX phase is scaled by a factor of 2 for a clearer view. **(e)** PDF refinement of the sample collected at the end of 11th charge using one single phase (Cr_2O_3), where the difference pattern (green) shows an evident pattern of a DRX phase, confirming its presence.

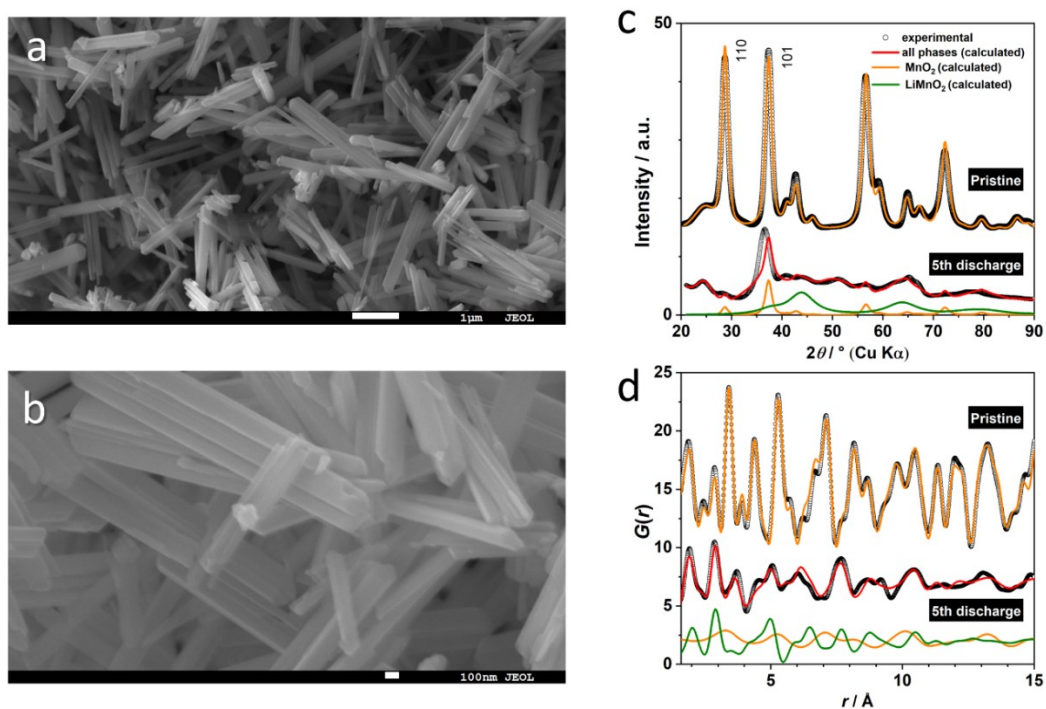


Figure S8 (a-b) SEM image of the nanostructured β - MnO_2 prepared by hydrothermal synthesis. Joint refinement of *ex situ* **(c)** XRD and **(d)** PDF data collected at the selected states of (dis)charge. Note that a stronger relative peak intensity was observed for the (101) reflection, in line with the rod-like morphology, indicating a preferred orientation of the particle.

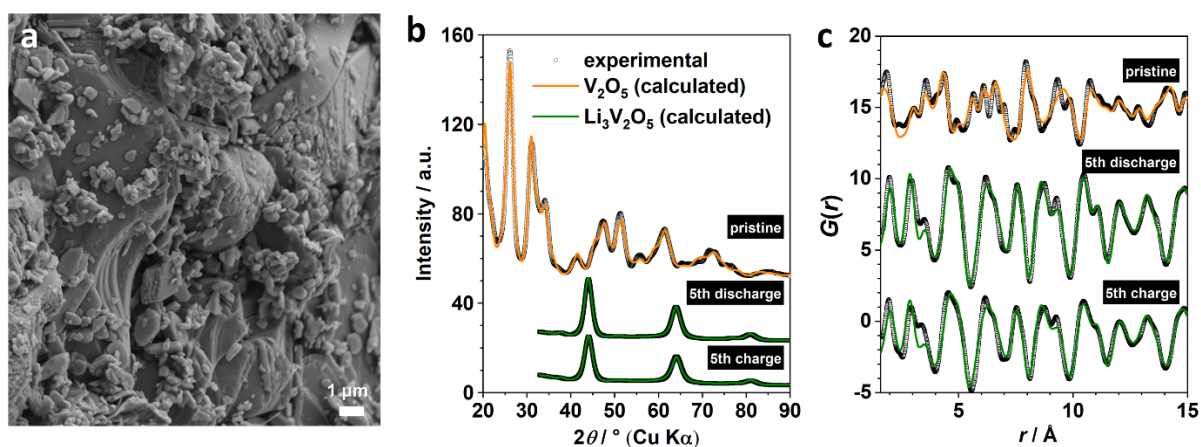


Figure S9 (a) SEM image of the commercial V_2O_5 . Refinement of *ex situ* **(b)** XRD and **(c)** PDF data collected at the selected states of (dis)charge. Full conversion to a DRX phase is evident after cycling.

References:

1. Y. Dong, K. Li, P. Jiang, G. Wang, H. Miao, J. Zhang and C. Zhang, *RSC Advances*, 2014, **4**, 39167-39173.
2. H. S. Geddes, H. Blade, J. F. McCabe, L. P. Hughes and A. L. Goodwin, *Chem. Commun. (Cambridge, U. K.)*, 2019, **55**, 13346-13349.
3. D. D. Lee and H. S. Seung, *Nature*, 1999, **401**, 788-791.
4. T. Egami and S. J. L. Billinge, *Underneath the Bragg Peaks Structural Analysis of Complex Materials*, Pergamon, Kidlington, Oxford, 2012.